Direct numerical simulation (DNS) modeling of PEFC electrodes Part II. Random microstructure

Guoqing Wang [1], Partha P. Mukherjee, Chao-Yang Wang [*]

*Electrochemical Engine Center (ECEC), Department of Mechanical & Nuclear Engineering,
The Pennsylvania State University, University Park, PA 16802, USA*

Abstract

The direct numerical simulation (DNS) method, developed for modeling the cathode catalyst layer (CL) of a polymer electrolyte fuel cell (PEFC) in Part I, is further extended wherein the catalyst layer is described as a random three-dimensional porous structure. A random CL microstructure is obtained using a computer-generated random number with specified porosity and pore size as the input structural parameters. Some statistical features of the CL and their dependence on the porosity are identified and demonstrated. The charge and species conservation equations are solved directly on this microscopically complex structure. The results from the DNS calculation are compared with the one-dimensional macrohomogeneous predictions and the Bruggeman factor for transport property correction is evaluated, which can be used as direct input into the macroscopic fuel cell models.
© 2005 Elsevier Ltd. All rights reserved.

Keywords: Polymer electrolyte fuel cell; Cathode catalyst layer; Pore-level description; Direct numerical simulation (DNS); Random microstructure

1. Introduction

In our companion paper [1], a regular microstructure was constructed to represent the simplified three-dimensional cathode catalyst layer for application of the DNS model. The regular 3-D structure, although offering an improvement over the two-dimensional geometry, suffers from many morphological and associated physical limitations. Besides the simplicity of the structure, statistical information still deviates from a realistic porous catalyst layer. For instance, the phase interfacial area needs to be further enhanced; the constituent phases are not as tortuous as that in a practical porous medium. In this work, a random porous microstructure is constructed and the DNS model is implemented systematically. The structural and transport characteristics are investigated subsequently.

The general objective of constructing a random microstructure is to mimic more closely the statistical nature of a real porous medium or the random arrangement of pores and solids at the

microscopic scale. This method enables us to create "digital" microstructures with desired properties. As a general procedure, certain low-order statistical properties (e.g., porosity and two-point correlation function) of the real porous medium are measured experimentally first and a synthetic medium is reconstructed having the same average parameters. The numerical reconstruction of a two-dimensional random porous medium with specified porosity and autocorrelation function was originally developed by Joshi [2] and further extended to three-dimension by Quiblier [3]. This statistics-based microstructure generation method was slightly modified by Ioannidis et al. [4] by using Discrete Fourier Transform, originally devised by Gutjahr [5]. Adler et al. [6] applied the stochastic reconstruction method to generate Fontainbleau sandstone microstructure. Briefly, the stochastic simulation technique is based on the truncation of Gaussian random fields and is capable of generating synthetic pore spaces with specified porosity and correlation function.

In this work, a 3-D purely random porous structure with a given porosity and pore size is reconstructed and subsequently used for the DNS model. The numerical reconstruction procedure of the catalyst layer microstructure is described first. Some statistical features of the microstructure and their dependence on

* Corresponding author. Tel.: +1 814 863 4762; fax: +1 814 863 4848.
 E-mail address: cxw31@psu.edu (C.-Y. Wang).
 [1] Present address: Plugpower Inc., 968 Albany-Shaker Road, Latham, NY 12110, USA.

the given porosity are subsequently identified and demonstrated. A modified DNS model is further presented for this microscopically complex structure, based on the 3-D DNS model described in the companion paper [1]. Finally, after solving the charge and oxygen conservation equations directly on the simulated random catalyst layer, the DNS results are compared with the predictions from a one-dimensional macrohomogeneous model, from which the Bruggeman factor for transport property correction is evaluated and limitations of the macrohomogeneous model are also discussed.

2. Random structure

2.1. General concept

Except for a few man-made microstructures, most of the real porous media are random. However, the qualifier "random" is quite obscure and can be applied to delineate very different situations, such as pure disorder and correlated disorder in a porous medium and hence needs further clarification.

Ideally, each point $\mathbf{r}$ within the 3-D space of an arbitrarily complex porous structure can be designated as either belonging to the void phase ($\mathbf{r} \in V_r$) or to the solid phase ($\mathbf{r} \in S_r$). The pore structure can then be completely defined in terms of a binary phase function $Z(\mathbf{r})$, which takes discrete values in the 3-D space according to the following definition [7]:

$$Z(\mathbf{r}) = \begin{cases} 1 & \text{if } \mathbf{r} \in V_r \\ 0 & \text{if } \mathbf{r} \in S_r \end{cases} \tag{1}$$

The first two moments of the phase function are the porosity, ε, and the autocorrelation function, $R_Z(\mathbf{u})$, defined respectively as [7]:

$$\varepsilon = \langle Z(\mathbf{r}) \rangle \tag{2}$$

$$R_Z(\mathbf{u}) = \frac{\langle [Z(\mathbf{r}) - \varepsilon][Z(\mathbf{r} + \mathbf{u}) - \varepsilon] \rangle}{\varepsilon - \varepsilon^2} \tag{3}$$

where angular brackets denote statistical averages and $\mathbf{u}$ is a lag vector. For a statistically homogeneous porous medium, ε is a constant and $R_Z(\mathbf{u})$ is only a function of the separation/lag vector, $\mathbf{u}$, and does not depend on the spatial coordinates (i.e. independent of $\mathbf{r}$). Physically, the two-point autocorrelation function refers to the probability that two points at a distance, $\mathbf{r}$, are both in the pore space. In addition, if the medium is isotropic, then the autocorrelation function does not depend on the direction but only on the modulus, u, of the vector $\mathbf{u}$. Furthermore, for a purely disordered porous medium, the autocorrelation function is independent of u and identically goes to zero. In such a porous structure, each elementary cube (voxel) resulting from the discretization of the 3-D continuum space is occupied at random either with the solid phase or the void phase with a given probability, ε and can be realized, in principle, by throwing a dice. This simplest construction rule is employed here to generate the catalyst layer microstructure for the DNS model, which is elaborated in the following section.

2.2. Numerical reconstruction

Numerical reconstruction is a unique approach that enables the prediction of macroscopic properties from the microscopic structure and the underlying pore-scale physics of a real, thus random porous medium [7]. In principle, this method consists of three major steps. The first step is the experimental measurement of some statistical features describing the microstructure. Often, the first two popular low-order moments (i.e. porosity and autocorrelation function) are measured. The second step is the numerical reconstruction of random porous medium in such a way that on average the generated microstructure possesses the same statistical features as the real porous medium. Once the microstructure is generated, all the transport processes can be studied in principle. In the case of the DNS model, by defining a phase function [1], a single set of transport equations valid for the entire microstructure can be solved.

In the current work, a purely random porous medium is computer-generated by employing a random number generator instead of following the first two steps described above. The porosity, ε and pore size, d are chosen as the target geometry features for the microstructure to match. Specifically, the porous catalyst layer is constructed in a discrete manner. It is considered to be composed of $N_x \times N_y \times N_z$ cubes, each of the same size d, which represents the chosen pore scale. These elementary cubes are filled with either the electrolyte phase or the pore phase. Similar to the approach in our previous work [1], a mixed electrolyte/electronic phase is considered which is justified later and henceforth referred to as the electrolyte phase in the rest of the paper. During reconstruction, the computer generates a random number uniformly distributed within the interval [0, 1] for each cube. When the random number is lower than the given porosity, ε, the corresponding cube is set to be occupied by the pore phase. Otherwise, it is occupied by the electrolyte phase.

2.3. Structural analysis and identification

Once the microstructure is constructed, structural connectivity needs to be imposed by forming pore clusters consisting of a group of connected pores. When the porosity, ε, is small, the pores form small and isolated clusters. When ε is large enough, among the pore clusters, there would be one that penetrates the entire medium from one end to the other. This kind of pore cluster is termed as "transport" pore cluster, since it forms a continuous network allowing the fluid to transport across the entire medium. In other words, the porous medium is permeable only if such a "transport" pore cluster exists. A pore belonging to the "transport" pore cluster is called a "transport" pore; otherwise it is called a "dead" pore. Apparently, as ε increases, there would be fewer and fewer "dead" pores and as ε is close to one, all the pores would be "transport" pores.

The constructed random cathode catalyst layer structure for the present work is shown in Fig. 1. The elementary cube size is $0.25\,\mu m$, representing the chosen pore size. Therefore, to simulate the $10\,\mu m$ thick catalyst layer, 40 cubes are applied in the thickness direction. Similar to the approach in the companion paper [1], one cube layer of only electrolyte and one layer
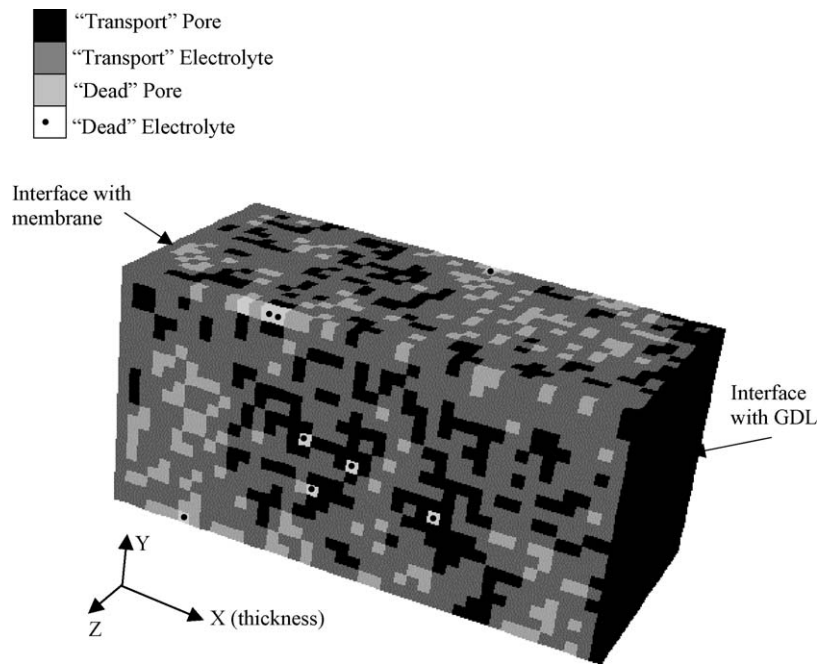
Fig. 1. Schematic diagram of the 3-D random catalyst layer microstructure with nominal porosity of 0.36.

of only pore are added to the left and right boundaries of the computational domain, respectively, for ease of implementation of the boundary condition. To investigate transport properties of the constructed random microstructure, the "transport" and "dead" portions of each phase have been numerically identified, as shown in Fig. 1 and the process of designation is detailed below.

The numerical approach of identifying the "transport" and "dead" portions for each phase starts with assigning an initial value of a phase function, f, to each elementary control volume in the entire computational domain. On the left boundary of electrolyte-only cells, f is set to be one; while f is assigned to be zero within the pore-only cells on the right boundary. Elsewhere within the domain, f is assigned three inside the electrolyte cells and two inside the pore cells. Then starting from the left boundary, each constituent elementary control volume is scanned to identify the "transport" electrolyte. For the cell with f equal to three, if any of its six neighboring cells has f equal to one, the phase function, f of the cell itself is switched to one. After each scan of the entire domain, the total number of cells with f equal to three is counted. The scan from left to right is repeated until the total number of cells having phase function value of three does not change anymore. Thus the cells with f equal to one are identified as "transport" electrolyte; while those with f equal to three represent "dead" electrolyte. Similarly, for the pore phase, the scanning process is continued from right boundary to the left and once a cell with f equal to two has any neighboring cell with f equal to zero, the value of the phase function, f of the cell itself is switched to zero. Finally, after sufficient number of scans, the cells with f equal to zero and two are identified as "transport" and "dead" pores, respectively.

The "transport" pore and the "transport" electrolyte identified here represent those elementary control volumes which are accessible for oxygen from the gas diffusion layer (GDL) at the right boundary and the protons from the polymer electrolyte membrane at the left boundary, respectively. In Fig. 1, the identified "transport" pore and "transport" electrolyte, as well as "dead" pore and "dead" electrolyte are indicated with different gray cubes, corresponding to a natural porosity of 0.36. As expected, there are few "dead" electrolyte cells since the electrolyte volume fraction is relatively large (0.64). On the other hand, only about 70% of total pores are identified as "transport" pores, indicating the effective "transport" porosity is only about 0.26.

The constructed random microstructure, shown in Fig. 1, includes 20 elementary cubes in y and z directions each, while the simulated catalyst layer is considered isotropic and periodic in y and z directions. Fig. 2 shows the dependence of the effective porosity on the number of cells included in the y and z directions. It shows that when the total number of cells in the y and z directions is doubled from 20 to 40, the "transport" pore volume fraction varies only slightly if the natural porosity is greater than 0.3. Since the range of porosity smaller than 0.3 is not realistic for practical applications of the catalyst layer, the number of cells of 20 is chosen to be sufficient in the y and z directions and employed for all the subsequent DNS calculations.

Fig. 3 shows the effective porosity and phase interfacial area ratio as a function of the natural porosity. The phase interfacial area ratio is defined as the ratio of the interfacial area in a porous structure to the cross-sectional geometrical area. Here the total interfacial area ratio represents all interfaces between the electrolyte and pore phases, while the active interfacial area ratio only includes those between "transport" electrolyte and "transport" pores, indicating that the interfacial sites are accessible by protons, electrons and oxygen and hence undergo the electrochemical reaction. The figure only shows the natural porosity
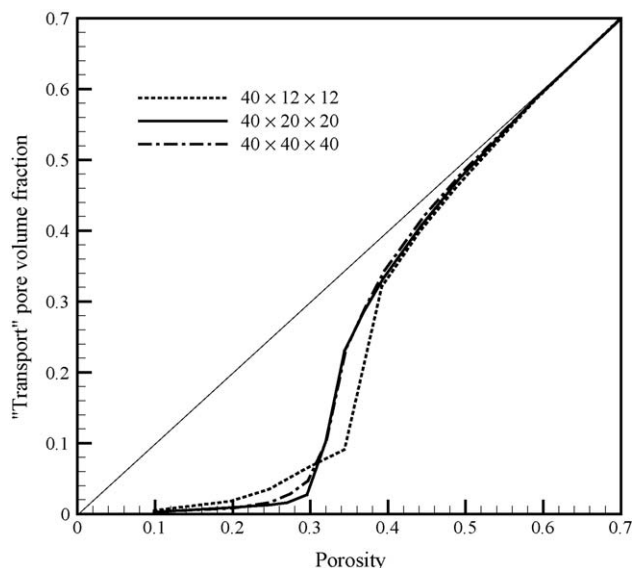
Fig. 2. Effect of cross-sectional mesh resolution on the transport pore volume fraction.

range up to 0.6 because the effective porosity is nearly identical to the natural porosity when it is larger than 0.6. Note that the interfacial area curve is symmetric around the porosity of 0.5. It is also seen that when the porosity is smaller than 0.35, both effective porosity and active interfacial area are reduced dramatically. This is of significance in practical applications, indicating that 0.35 is the lower bound of the porosity for the catalyst layer. Furthermore, the random microstructure provides a realistic active interfacial area ratio of between 40 and 50, which has been significantly improved compared to that with the 3-D regular microstructure simulation in the companion paper [1]. This value of the reaction area ratio corresponds roughly to 0.15 mg Pt/cm^2 catalyst loading with a dispersion surface area of Pt particles at 35 m^2/g Pt, which is representative in current applications.
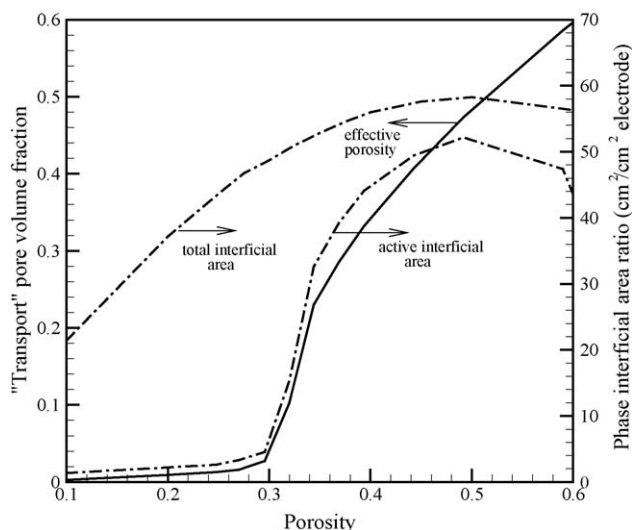

Fig. 3. Variation of transport pore volume fraction and phase interfacial area ratio with nominal porosity.
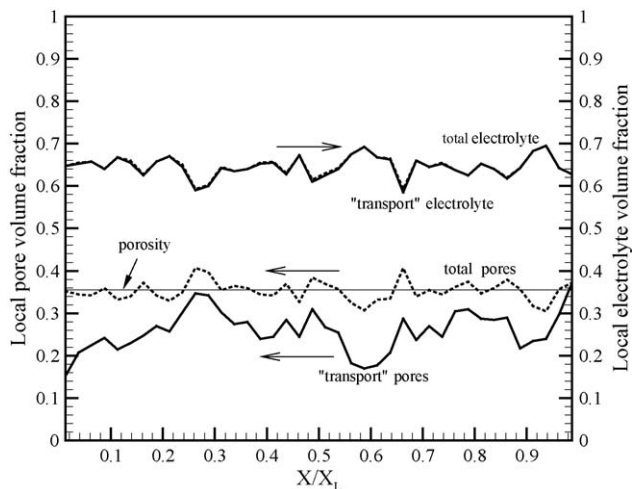

Fig. 4. Profiles of pore and electrolyte volume fractions along the thickness of the catalyst layer.

The local pore and electrolyte distributions across the thickness of the catalyst layer are shown in Fig. 4. First, the local cross-sectional averaged natural porosity shows a random fluctuation around the average porosity of the entire porous structure marked by the horizontal line. Secondly, most of the electrolyte cells are available for transport, while a considerable portion of pores are dead pockets. The percentage of "transport" pores distributes uniformly in most locations except for the front and back end of the structure. At the backside (i.e. near the left boundary) of the catalyst layer interfacing with the membrane, more pores are "dead" indicating difficulty of oxygen access. On the other hand, at the frontside (i.e. near the right boundary) interfacing with the GDL, there are mostly "transport" pores partly because the structure is open to large pore space in the GDL.

3. DNS model

3.1. Governing equations

The DNS model, developed for the 3-D regular CL microstructure in our companion paper [1], is extended here to solve the charge and oxygen concentration conservation equations on the random 3-D microstructure. The basic model assumptions remain the same as in Part I [1]. The meaning of the symbols can be found in the nomenclature.

The discrete phase function, f, introduced in Part I [1] for the single-domain approach, is redefined for the elementary control volumes within the computational domain as:

$$f(i, j, k) = \begin{cases} 0 & \text{``transport'' pores} \\ 1 & \text{``transport'' electrolytes} \\ 2 & \text{``dead'' pores} \\ 3 & \text{``dead'' electrolytes} \end{cases} \qquad (4)$$

Correspondingly, the proton conductivity and oxygen diffusivity can be expressed in terms of the phase function, in the discretized

fashion, as:

$$K(i, j, k) = \{\kappa \times f(i, j, k) \times [2 - f(i, j, k)] \times [3 - f(i, j, k)]\} / 2 \tag{5}$$

$$D_{O_2}(i, j, k) = \left\{ D_{O_2}^g \times [1 - f(i, j, k)] \times [2 - f(i, j, k)] \right.$$
$$\left. \times [3 - f(i, j, k)] \right\} / 6 \tag{6}$$

From the above expressions it is obvious that the proton conductivity and oxygen diffusivity identically go to zero in the "dead" electrolyte and the "dead" pore cells respectively.

The governing differential equations for the conservation of charge and oxygen transport, as detailed in the companion paper, Part I [1], can be readily extended to be valid throughout the domain by suitably expressing the source terms using the discrete phase function, $f(i, j, k)$. The source terms for charge and oxygen transport, S_ϕ and S_{O_2}, respectively, are defined at the cell center (i, j, k) of the "transport" electrolyte and "transport" pore cells next to each other, respectively, forming the active catalyzed interface where the electrochemical reaction occurs. The source terms in the discretized form can be expressed as:

$$S_\phi(i, j, k) = -\frac{i_0}{c_{O_2,\text{ref}}^g} f(i, j, k) \exp\left[\frac{\alpha_c F}{RT}\phi_e(i, j, k)\right] \times \left\{ [1 - f(i-1, j, k)]\frac{c_{O_2}(i-1, j, k)}{\Delta x} + [1 - f(i+1, j, k)]\frac{c_{O_2}(i+1, j, k)}{\Delta x} \right.$$
$$+ [1 - f(i, j-1, k)]\frac{c_{O_2}(i, j-1, k)}{\Delta y} + [1 - f(i, j+1, k)]\frac{c_{O_2}(i, j+1, k)}{\Delta y} + [1 - f(i, j, k-1)]\frac{c_{O_2}(i, j, k-1)}{\Delta z}$$
$$\left. + [1 - f(i, j, k+1)]\frac{c_{O_2}(i, j, k+1)}{\Delta z} \right\} \tag{7}$$

$$S_{O_2}(i, j, k) = -\frac{i_0}{4F c_{O_2,\text{ref}}^g}[1 - f(i, j, k)]c_{O_2}(i, j, k) \times \left\{ f(i-1, j, k)\frac{\exp[(\alpha_c F/RT)\phi_e(i-1, j, k)]}{\Delta x} + f(i+1, j, k) \right.$$
$$\times \frac{\exp[(\alpha_c F/RT)\phi_e(i+1, j, k)]}{\Delta x} + f(i, j-1, k)\frac{\exp[(\alpha_c F/RT)\phi_e(i, j-1, k)]}{\Delta y} + f(i, j+1, k)$$
$$\times \frac{\exp[(\alpha_c F/RT)\phi_e(i, j+1, k)]}{\Delta y} + f(i, j, k-1)\frac{\exp[(\alpha_c F/RT)\phi_e(i, j, k-1)]}{\Delta z} + f(i, j, k+1)$$
$$\left. \times \frac{\exp[(\alpha_c F/RT)\phi_e(i, j, k+1)]}{\Delta z} \right\} \tag{8}$$

The transfer current between the two neighboring cells forming an active interface is given by the Tafel equation, which is justified due to the small value of the exchange current density of the ORR:

$$j = i_0 \frac{c_{O_2}(i+1, j, k)}{c_{O_2,\text{ref}}^g} \exp\left[\frac{\alpha_c F}{RT}\phi_e(i, j, k)\right] \quad (\text{A/cm}^2) \tag{9}$$

where $\phi_e(i, j, k)$ represents the cathode overpotential since both the open-circuit potential and the electronic phase potential are assumed constant. The prefactor, i_0, is the modified exchange current density as detailed in Part I [1]. It should be borne in mind that the transfer current density, j, is negative for the electrolyte phase.

In the present simulation, the proton conductivity is adjusted using a Bruggeman type correlation to correct for the mixed electrolyte/electronic phase according to the following expression:

$$\kappa = \kappa_0 \times \left(\frac{\varepsilon_e}{\varepsilon_e + \varepsilon_s}\right)^{1.5} = \kappa_0 \times \left(\frac{\varepsilon_e}{1 - \varepsilon_g}\right)^{1.5} \tag{10}$$

where κ_0 is the intrinsic conductivity of the electrolyte, ε_e, ε_s and ε_g are the electrolyte, electronic and pore volume fractions, respectively. In this study, the intrinsic ionic conductivity, κ_0, is considered to be constant since the membrane is assumed fully humidified.

3.2. Boundary conditions

The boundary conditions used in the present simulation remain the same as in the case of a regular 3-D catalyst layer microstructure, described in Part I [1], except for the oxygen concentration, $c_{O_2,0}$, at the CL–GDL interface. In the previous study, the mass transport resistance in the GDL was ignored and the oxygen concentration at the channel inlet was directly applied on the right boundary i.e. at the CL–GDL interface. In this work, the oxygen concentration drop in the GDL is further included in order to provide a more realistic boundary condition.

The oxygen concentration in the gas channel is assumed uniform, as shown schematically in Fig. 5, which physically corresponds to a large stoichiometric flow rate. By employing an effective oxygen diffusivity, $D_{O_2,\text{GDL}}^{g,\text{eff}}$, through the GDL, the oxygen flux at the CL–GDL interface can be written as:

$$N_{O_2} = D_{O_2,\text{GDL}}^{g,\text{eff}} \times \frac{c_{O_2,\text{inlet}} - c_{O_2,0}}{\Delta X_{\text{GDL}}} \tag{11}$$

where ΔX_{GDL} refers to the thickness of the GDL. The porosity, ε_{GDL} and tortuosity, λ_{GDL} of the GDL are employed to define
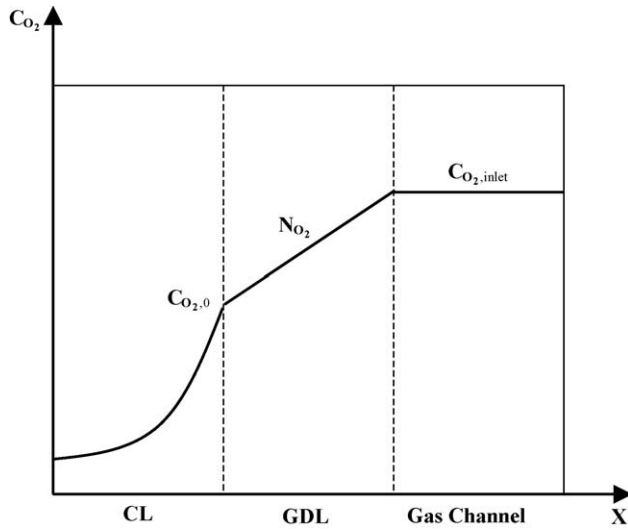
Fig. 5. Schematic diagram of the oxygen concentration profile in the cathode.

the effective oxygen diffusivity as:

$$D_{O_2,GDL}^{g,eff} = D_{O_2}^g \times \frac{\varepsilon_{GDL}}{\tau_{GDL}} \tag{12}$$

$D_{O_2}^g$ is the intrinsic oxygen diffusivity which in turn depends on the specified pressure and temperature as [8]:

$$D_{O_2}^g = D_{O_2,0}^g \left(\frac{T}{T_0}\right)^{3/2} \left(\frac{p_0}{p}\right) \tag{13}$$

At steady state, the total flux through the GDL should be equivalent to the oxygen consumption rate at the catalyst layer, that is:

$$N_{O_2} = \frac{I}{4F} \tag{14}$$

Thus, the oxygen concentration at the catalyst layer–GDL interface can be derived by combining Eqs. (11) and (14) and is given by:

$$c_{O_2,0} = c_{O_2,inlet} - \frac{I \times \Delta X_{GDL}}{4F \times D_{O_2,GDL}^{g,eff}} \tag{15}$$

It is evident that the corrected oxygen concentration depends not only on the inlet oxygen concentration but also on the concentration drop through the GDL. At large operating current densities, there could be a considerable drop across the GDL due to the large oxygen flux.

The model input parameters including the properties of the GDL are summarized in Table 1.

3.3. Solution methodology

The user defined functions (UDF) capability in the commercial CFD software, Fluent® [9], was systematically deployed to solve the conservation equations for charge and oxygen transport with proper attention to handling of the source terms as given by Eqs. (7) and (8). Convergence was considered achieved for each scalar field when the relative error between two successive iterations reached 10^{-6}.

Table 1
Model input parameters

Parameter	Value
Proton conductivity of the fully hydrated membrane, $\kappa_{e,0}$ (S/m)	12.3
Reference intrinsic oxygen diffusivity, $D_{g,0}^{O_2}$ (m²/s)	3.2×10^{-5}
Pressure at the channel inlet, p (kPa)	150
Operating temperature, T (°C)	80
Thickness of the GDL, ΔX_{GDL} (μm)	300
Porosity of the GDL, ε_{GDL}	0.4
Tortuosity of the GDL, τ_{GDL}	4
Natural porosity of the catalyst layer, ε_g	0.36
Electrolyte volume fraction in the catalyst layer, ε_e	0.3

4. Results and discussion

4.1. Three-dimensional potential and oxygen concentration fields

DNS simulations with varying operating current density were carried out on the computer-generated random microstructure of the cathode catalyst layer. The predicted polarization curve is shown in Fig. 6. As expected, the predicted polarization curve has a fast drop in the small current density region controlled by the ORR kinetics followed by a linear voltage drop in the mixed kinetic-ohmic control regime and finally at current densities larger than 1.5 A/cm², the mass transport limitation appears with a fast voltage drop resulting from oxygen depletion.

Fig. 7 compares the characteristics of oxygen transport at different current densities. Three-dimensional contours of the oxygen concentration are plotted for 0.5, 1.5 and 2.0 A/cm² current densities. The oxygen concentration at the right boundary (i.e. the CL–GDL interface) assumes a different value depending on the operating current density as evident from Eq. (17). The larger the current density, the greater is the gradient in the oxygen concentration through the GDL. Thus, the oxygen concentration at the CL–GDL interface becomes increasingly smaller with
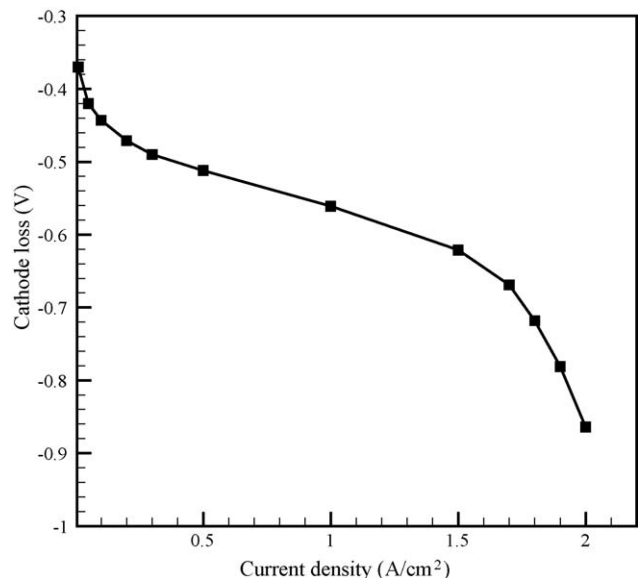

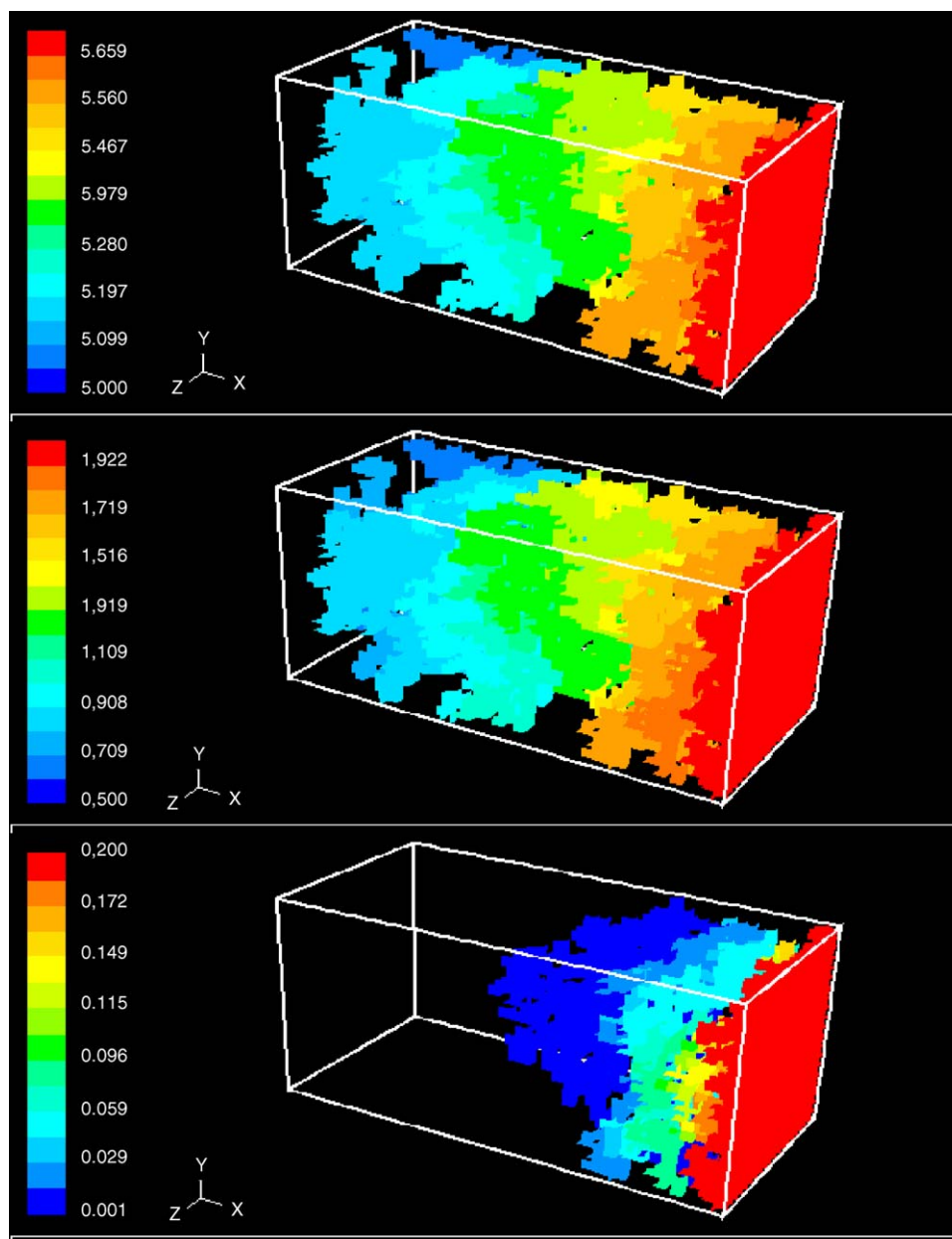Fig. 6. Polarization curve predicted by the DNS calculation.

Fig. 7. 3-D contours of the oxygen concentration (mol/m^3) at 0.5, 1.5 and 2.0 A/cm^2 current densities, respectively, from top to bottom.

the increase in the current density despite the constant oxygen concentration at the channel inlet. At the current density of 0.5 A/cm^2, the cross-sectional averaged oxygen concentration is fairly uniform, varying from 5.1 to 5.6 mol/m^3 across the catalyst layer thickness. When the current density is increased to 1.5 A/cm^2, due to both the mass transport resistance in the GDL and large consumption rate, the concentration in the vicinity of the membrane–CL interface diminishes leading to a nearly oxygen depleted zone. Upon further increase in current density to 2.0 A/cm^2, it is observed that oxygen depletion occurs in most of the region of the catalyst layer, resulting in a very narrow reaction zone next to the CL–GDL interface.

The corresponding reaction current distributions are displayed in Fig. 8. As expected, it shows a uniform reaction rate across the thickness of the catalyst layer at 0.5 A/cm^2; while at

the large current density of 2.0 A/cm^2, the reaction is confined to a narrow zone toward the front end where oxygen is available. The reaction current distribution at the current density of 1.5 A/cm^2 is particularly unique in the sense that the reaction rate is higher at both ends than that in the middle section. It is believed that the combined effects of oxygen concentration and electrolyte potential distributions lead to this special reaction current profile. Near the membrane end, the large reaction rate is due to the greater overpotential, while toward the GDL end, the high reaction rate is not only due to the high concentration of oxygen but also due to the availability of more "transport" pores. A clearer picture is provided in Fig. 9 where the cross-sectional averaged reaction current is displayed across the catalyst layer thickness. The local "transport" pore volume fraction is also included in the same figure to elucidate the effect of the local
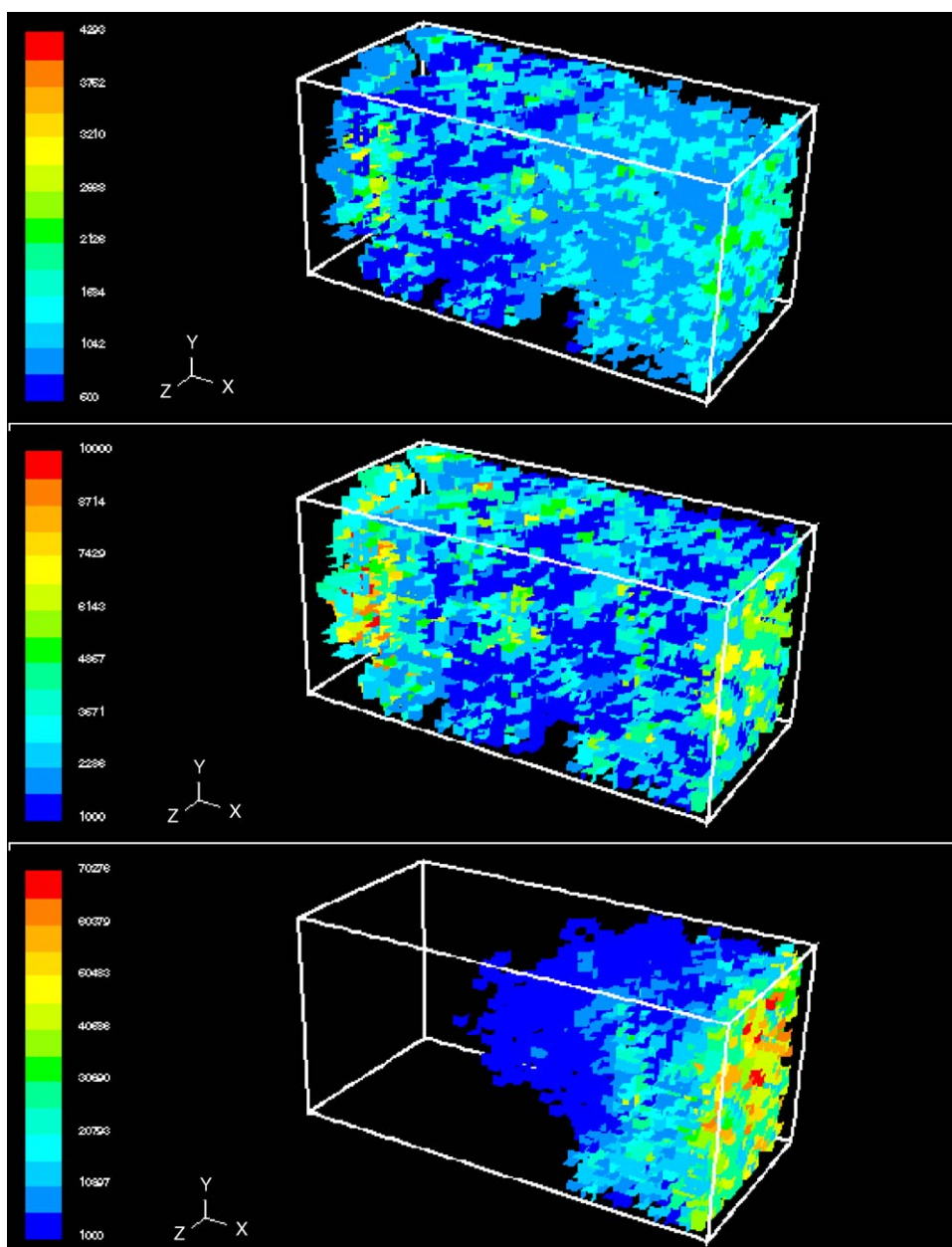
Fig. 8. 3-D contours of the reaction current (A/m^2) at 0.5, 1.5 and 2.0 A/cm^2 current densities, respectively, from top to bottom.

porosity variation. It can be clearly seen that the local reaction current oscillates following the local "transport" pore volume fraction. Obviously, more transport pores essentially lead to a greater interfacial active area for reaction, resulting in a larger reaction rate.

4.2. Comparison between the DNS and 1-D macrohomogeneous model results

One of the major implications of constructing a random microstructure is to provide phase interfacial area and tortuosity comparable to that of a real catalyst layer microstructure. Therefore, solving point-wise conservation equations on a realistic structure, we can, in essence, evaluate the Bruggeman correlations required for macrohomogeneous models. Bruggeman

correction factor, ξ, is commonly applied to determine the effective transport properties as follows:

$$\Gamma_k^{\text{eff}} = \Gamma_k \times \varepsilon_k^{\xi} \tag{16}$$

In the 1-D macrohomogeneous model, the same specific surface area a (cm^2/cm^3) as that in the constructed random structure is used in the Butler–Volmer equation to represent the volumetric reaction current, that is:

$$j = a \times i_0 \left[\exp\left(\frac{\alpha_a F}{RT} \eta \right) - \exp\left(-\frac{\alpha_c F}{RT} \eta \right) \right] \quad (\text{A/cm}^3) \tag{17}$$

The comparison of polarization curves predicted by the DNS and 1-D macrohomogeneous models is shown in Fig. 10. Three different Bruggeman factors, 1.5, 3.5 and 4.5, are attempted. It
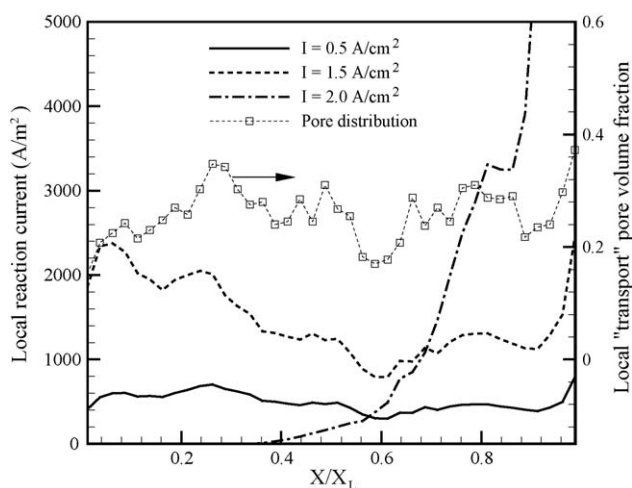
Fig. 9. Reaction current and effective porosity distributions across the catalyst layer thickness at different current densities.

Fig. 11. Comparison between the cross-sectional averaged oxygen concentration profiles from the DNS and 1-D macrohomogeneous model predictions.

can be seen that at small current densities (up to ∼1 A/cm^2), a factor of 3.5 gives a good agreement to the DNS predictions; while in the large current density regime, a value of the Bruggeman factor between 3.5 and 4.5 is suggested. Detailed comparisons at the current density of 1.5 A/cm^2, such as the oxygen concentration distribution, electrolyte phase potential and local reaction current distributions are depicted in Figs. 11–13, respectively.

In the case of the oxygen concentration (Fig. 11), the DNS result is in good agreement with the 1-D homogeneous model prediction with the Bruggeman factor of 4.5. However, Fig. 12 shows that the factor of 3.5 gives a better match for the shape of the overpotential curve except that the DNS result is about 12 mV higher consistently. The higher surface overpotential stems from the lower active interfacial area in the DNS model. It can be seen from Fig. 3 that there are only about 65% of the total interfacial area that is active for the electrochemical reaction.
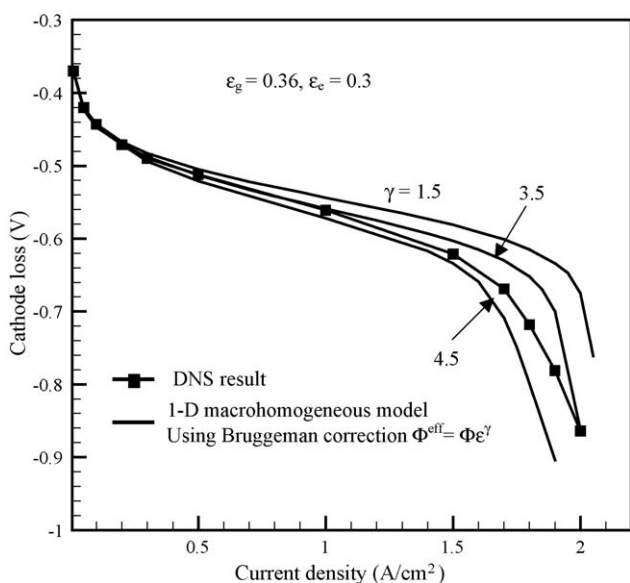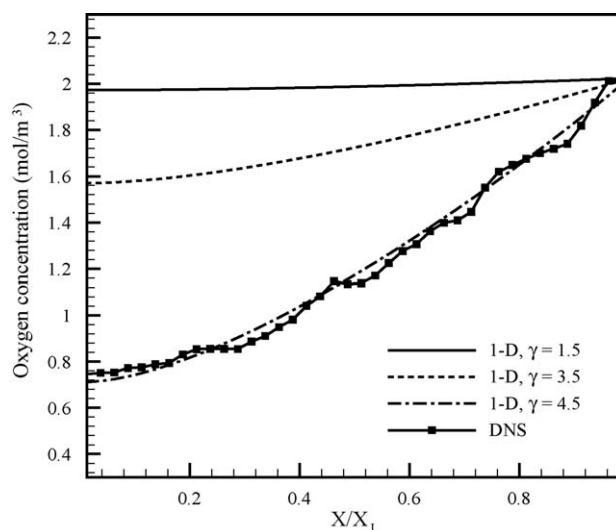
Combination of the findings from Figs. 11 and 12 suggest that the phase with low volume fraction, i.e. the gas phase in the present study, prefers a higher Bruggeman factor. This could be not only because of less tortuosity but also because of a lower effective porosity than the natural porosity for the gas phase. If using the effective porosity of 0.26 in the Bruggeman correction instead of the natural porosity 0.36, the Bruggeman factor would be about 3.4 (i.e. $0.26^{3.4} \approx 0.36^{4.5}$), very close to the value (i.e. 3.5) for the electrolyte phase. Another point worth noting is that the constructed 3-D microstructure features the influence of local variation in the effective porosity on the reaction current distribution; while the macrohomogeneous model only uses a constant natural porosity. As shown in Fig. 13, the DNS model generates a more uniform reaction current distribution than those of macrohomogeneous models with the Bruggeman factors of 3.5 and 4.5. As displayed in Fig. 4, although the natural pore volume fraction of this porous medium distributes uniformly around the average

Fig. 10. Comparison between the polarization curves from the DNS calculation and the 1-D macrohomogeneous model.
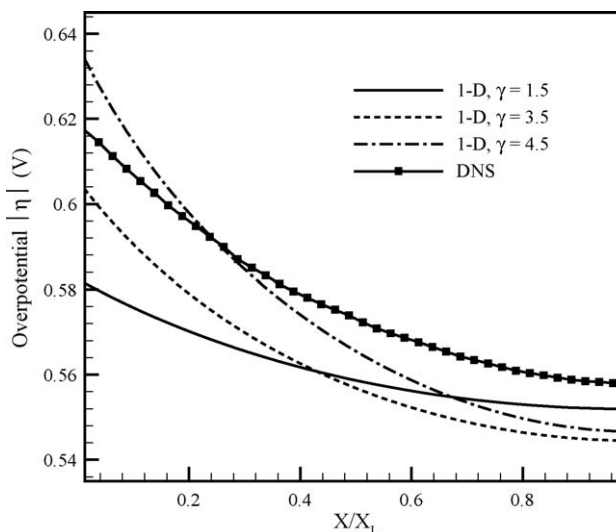

Fig. 12. Comparison between the cross-sectional averaged overpotential profiles from the DNS and 1-D macrohomogeneous model predictions.
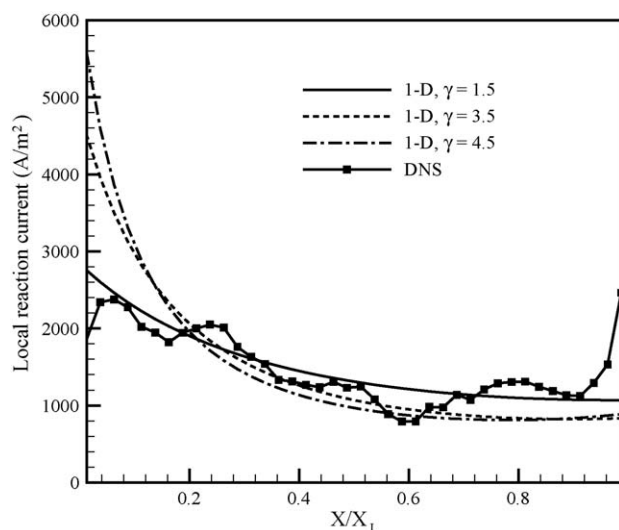
Fig. 13. Comparison between the cross-sectional averaged reaction current distributions across the thickness of the catalyst layer from the DNS and 1-D macrohomogeneous model predictions.

porosity, the effective porosity varies across the thickness of the catalyst layer. More "transport" pores toward the front end than near the back end makes a unique reaction current distribution that cannot be captured by the macrohomogeneous model using any Bruggeman correction factor.

5. Conclusions

Random nature of a porous catalyst layer is resolved by generating a purely disordered microstructure using a simplified variant of the stochastic approach. Influence of the microstructure properties (e.g. pore distribution) on the underlying transport phenomena and mutual interaction are demonstrated. The relative importance and influence of ionomer proton conduction and oxygen transport are clearly depicted by the reaction current distribution at different current densities. The distribution of the reaction current with the variation of the effective porosity across the catalyst layer thickness is uniquely captured by the DNS model, which is otherwise not delineated by the macrohomogeneous models. Finally, the Bruggeman correction factor ($\sim$3–3.5) evaluated from the DNS calculation is a valuable input to the macroscopic fuel cell models and hence underscores the striking advantages of the DNS method over the macrohomogeneous models.

Acknowledgement

Appendix A

Nomenclature

a	specific interfacial area (cm^2/cm^3)
c_i	local concentration of species i (mol/m^3)
d	pore size (µm)
D_i	diffusion coefficient of species i (m^2/s)
f	phase function for the single-domain approach
F	Faraday's constant (96 487 C/mol)
i_0	exchange current density (A/cm^2)
I	current density (A/cm^2)
j	reaction current density (A/cm^2)
p	pressure (Pa)
R	universal gas constant (8.314 J/mol K)
R_Z	autocorrelation function
S	source term in the governing equations
T	absolute temperature (K)
x	x coordinate (µm)
y	y coordinate (µm)
z	z coordinate (µm)
Z	phase function for the definition of a porous medium

Greek letters

α_a	anodic transfer coefficient
α_c	cathodic transfer coefficient
ε_k	volume fraction of phase, k, in the catalyst layer
η	surface overpotential (V)
κ	electrolyte conductivity (S/m)
ξ	Bruggeman correction factor
Γ	physico-chemical property
ϕ_k	electrical potential in phase k (V)

Subscripts and superscripts

e	electrolyte phase
eff	effective
g	gas phase
GDL	gas diffusion layer
inlet	gas channel inlet
L	catalyst layer thickness
O_2	oxygen
ref	reference value
0	boundary value at the CL–GDL interface or initial/intrinsic value

References

[1] G. Wang, P.P. Mukherjee, C.Y. Wang, Electrochim. Acta 51 (2006) 3139–3150.
[2] M. Joshi, Ph.D. Dissertation, University of Kansas, Lawrence, Kansas, 1974.
[3] J.A. Quiblier, J. Coll. Interf. Sci. 98 (1984) 84.
[4] M. Ioannidis, M. Kwiecien, I. Chatzis, Proceedings of the SPE Petroleum Computer Conference, Houston, June 11–14, 1995.
[5] A.L. Gutjahr, Project Report, New Mexico Institute of Mining and Technology, Contract No. 4-R58-2690R, 1989.
[6] P.M. Adler, C.G. Jacquin, J.A. Quiblier, Int. J. Multiphase Flow 16 (4) (1990) 691.
[7] P.M. Adler, Porous Media: Geometry and Transports, Butterworth–Heinemann, Stoneham, MA, 1992.
[8] R.B. Bird, W.E. Stewart, E.N. Lightfoot, Transport Phenomena, 2nd ed., Wiley, New York, 2002.
[9] Fluent 6.1 UDF Manual, Fluent Inc., NH, USA.